Communications in Theoretical Physics

Commun. Theor. Phys. **75** (2023) 075702 (14pp) https://doi.org/10.1088/1572-9494/accf71

# Dynamic magnetic behaviors and magnetocaloric effect of the Kagome lattice: Monte Carlo simulations

**Wei-Chen Wu**[1], **Kai-Le Shi**[2,3] **and Wei Jiang**[1,2,3,*]

[1] School of Science, Shenyang University of Technology, Shenyang 110870, China
[2] School of Environmental and Chemical Engineering, Shenyang University of Technology, Shenyang 110870, China
[3] School of Materials Science and Engineering, Shenyang University of Technology, Shenyang 110870, China

E-mail: weijiang@sut.edu.cn

Received 2 February 2023, revised 21 April 2023
Accepted for publication 24 April 2023
Published 14 June 2023

### Abstract

Based on the Monte Carlo method, we examined the dynamic magnetic behaviors and magnetocaloric effect of a Kagome lattice subjected to the influence of time-dependent oscillating and time-independent magnetic fields. We used the Ising model to describe the Kagome lattice and study the dynamic order parameters, blocking temperature, internal energy, and phase diagrams. The results revealed that exchange coupling increases the stability of the system and the bias field induces order; however, the time-dependent oscillating magnetic field induces disorder. In addition, the magnetocaloric properties, changes in magnetic entropy, and relative cooling power of the Kagome lattice were investigated.

Keywords: magnetocaloric, dynamic order parameter, Kagome lattice, phase diagrams, Monte Carlo simulations

(Some figures may appear in colour only in the online journal)

## 1. Introduction

The Kagome lattice is a two-dimensional hexagonal network composed of corner-sharing triangles, the structure of which has received considerable attention from the scientific community since its inception. This lattice can bind electrons in a six-membered ring and generate flat bands, thereby introducing interesting physical phenomena in condensed-matter physics. For example, when the Fermi surface is on a flat band, the extremely high density of the electron states on this band allows the system to be spontaneously ferromagnetic, despite the small Coulomb interaction between the electrons [1–3]. Additionally, the flat band is a natural platform for the realization of the Wigner lattice [4, 5] because the kinetic quenching of, and interactions between, electrons are dominant in this band. In addition, the Kagome structure is applied to the studies on Bose–Einstein condensate [6], high-temperature fractional quantum Hall effect [4, 7, 8], high-temperature superconductivity [9, 10], and other properties based on flat bands.

Another important property of the Kagome lattice is its ability to generate frustrated spin [11, 12]. Frustrated spin systems frequently manifest as interesting physical phenomena associated with nontrivial spin orders. Therefore, this lattice has attracted much attention as an important method of studying spin-liquid or spin-ice systems. For example, research and analysis of a series of spin-liquid materials, such as $Y_3Cu_9(OH)_{19}Cl_8$, $CaCu_3(OH)_6Cl_2 \cdot 0.6H_2O$, and $YCu_3(OH)_6Cl_3$, were conducted by applying this lattice [13–16].

The experimental results associated with the preparation and study of Kagome structural materials are equally impressive. Szymczak *et al* experimentally measured the inelastic neutron scattering from $Co_3V_2O_8$ single crystals and the electron paramagnetic resonance of $Co^{2+}$ ions in $Mg_3V_2O_8$ single crystals [17]. The authors concluded that the magnetic anisotropy of (M = Co, Ni, Mn) step

---

[*] Author to whom any correspondence should be addressed.

oxides is mainly owing to single ions. Jiang *et al* [18] prepared two open-frame transition metal fluorophosphates, $(NH_4)M_3(PO_3F)_2(PO_2F_2)F_2$ (M = Mn and Co), possessing Kagome lattices and found that the Kagome topology of the material exacerbates magnetic frustration and exhibits an antiferromagnetic ground state. Furthermore, Fe-Sn alloys are typical Kagome materials. Lin *et al* [19] experimentally combined scanning tunneling microscopy, angle-resolved photoelectron spectroscopy, and first-principles calculations to confirm the existence of a flat-band electronic structure in the quasi-dimensional Kagome compound $Fe_3Sn_2$. The existence of a magnetic Dirac semimetal was experimentally demonstrated for the first time by the authors.

Magnetic and thermodynamic properties are equally popular areas of investigation in the study of Kagome lattice materials. The magnetic behavior of two-dimensional decorated Kagome lattices in the Ising model was studied by Si *et al* [20]. Ananikian *et al* [21] investigated the magnetic properties and entanglement of fluid $^3$He in a Kagome lattice. Their results demonstrated that the system exhibited diverse magnetic behaviors depending on the exchange parameters. Yerzhakov *et al* [22] investigated the thermodynamic characteristics of geometrically frustrated ABC-stacked antiferromagnetic Kagome layer films using Metropolis Monte Carlo (MC) simulations. Soldatov [23] investigated the diluted antiferromagnetic Ising model in magnetic fields on Kagome lattices and discussed the similarities and differences in the resulting magnetization curves. Owing to its simple implementation and versatility, the Ising model is beneficial for studying the magnetic behavior of nanostructured systems [24–26]. In addition, MC simulations allow the study of the magnetic behaviors and magnetocaloric effects of nano-systems [27–30]. In our previous study, we successfully described the magnetic and thermodynamic properties of a nanosystem using the Ising model [31–33]. Moreover, dynamic phase transitions and hysteresis loop behaviors have raised significant interest [34, 35]. This is because when a material is exposed to a dynamically-applied magnetic field (both biased and time-varying oscillatory fields), the system does not simultaneously respond to both fields, but the order of the magnetic moment depends on the oscillating field over time, leading to dynamic phase transitions [36, 37]. Vatansever and Polat [38] researched materials, including triangular lattice and ferromagnetic thin film systems, under biased and oscillating magnetic fields and found that the amplitude of the oscillating magnetic fields affected the dynamic critical properties of the system [39]. Ertaš *et al* observed the dynamic hysteresis line behaviors of Ising ferromagnetic systems and discussed the effect of temperature on exchange coupling and the dynamic hysteresis behaviors [40–42]. Cardona *et al* used the MC method to study the influence of relevant parameters, including the frequency and amplitude of the oscillating magnetic field, on the dynamic magnetic and thermodynamic properties of $La_{2/3}Ca_{1/3}MnO_3$ under a time-dependent magnetic field [43]. Gallardo *et al* used an analytical approach to analyze the dynamic phase transition of the kinetic Ising model in mean field approximation and found that the time-independent field components are conjugate fields with ordered parameters [44]. Studies of dynamic phase transitions such as these are important in recent magnetic research. Although many advances have been made in the theoretical studies on the magnetism of Kagome structural lattices, most of these studies have focused on constant applied magnetic fields. Based on the MC simulations, Z. D. Vatansever studied the effect of system sizes on dynamic phase transition behaviors of the Kagome lattice in the presence of a square-wave oscillating magnetic field. The results indicate that the phase transition temperature increases with the increase in system size [45]. In this study, based on a fixed system size, we used MC simulations to demonstrate the dynamic magnetic properties and magnetocaloric effect of a single-layer Kagome lattice under dynamic magnetic fields.

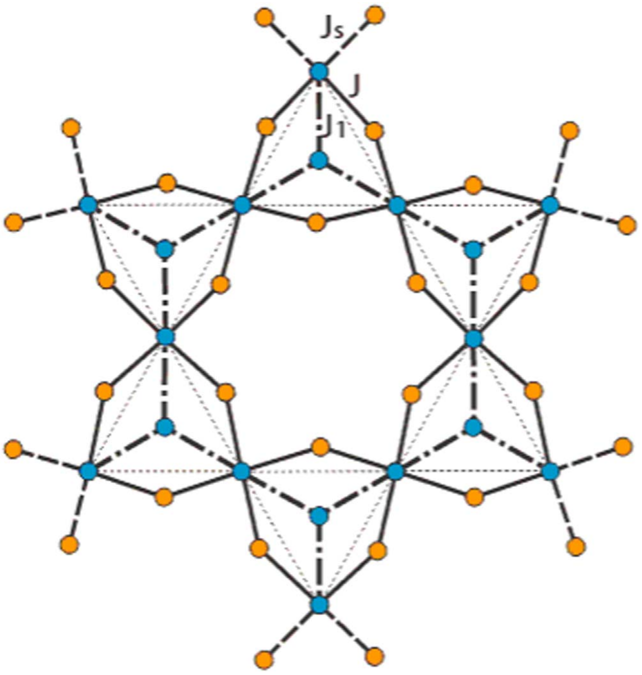

**Figure 1.** Diagram of the Kagome lattice. The yellow and blue balls represent magnetic atoms with spin −2 and spin −3/2, respectively. The dashed, solid and dash-dotted lines represent three types of exchange coupling $J_s$, $J$, and $J_1$, respectively.

The remainder of this paper is organized as follows. In section 2, we describe the model applied and briefly introduce the MC simulation. In section 3, we analyze the typical results obtained using the Kagome lattice model under different relevant parameters such as dynamic order, blocking temperature, internal energy, phase diagram and magnetocaloric effect. Finally, section 4 presents the conclusions of the study.

## 2. Model and Monte Carlo simulation

A schematic of a Kagome lattice is shown in figure 1. The lattice consists of two types of sublattices; the yellow and blue balls represent sublattices $A$ and $B$, respectively. The

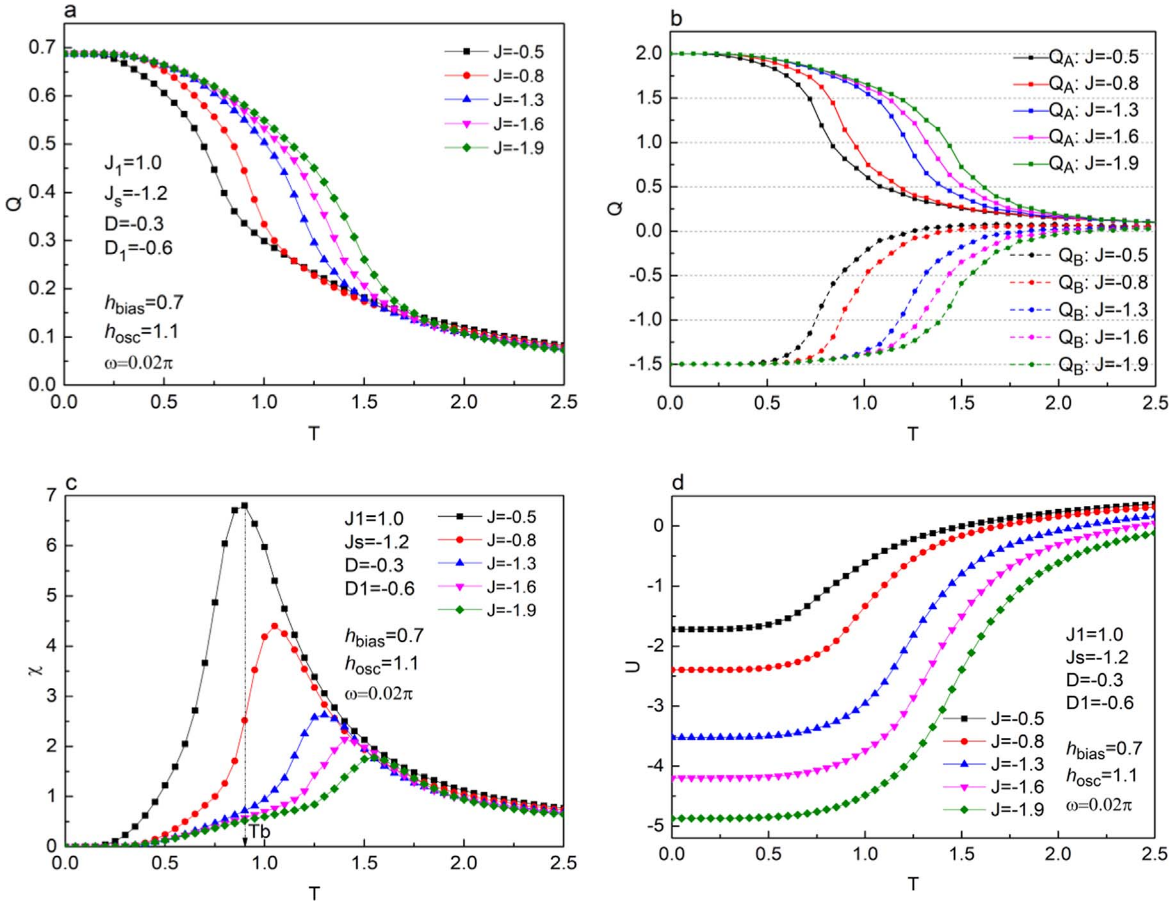

**Figure 2.** Temperature dependence of (a) the total dynamic order parameter $Q$, (b) dynamic order parameters $Q_A$ and $Q_B$, (c) susceptibility $\chi$, and (d) the internal energy $U$ for various $J$ with $J_s = -1.2$, $J_1 = 1.0$, $D = -0.3$, $D_1 = -0.6$, $h_{\rm bias} = 0.7$, $h_{\rm osc} = 1.1$ and $\omega = 0.02\pi$.

dash-dotted lines represent the nearest-neighbor ferromagnetic exchange couplings $J_1$ (>0). The dotted and solid lines represent the ferrimagnetic exchange couplings $J_s$ (<0) and $J$ (<0), respectively. Considering that the exchange coupling, anisotropy, and external magnetic field have significant influences on the system, the Hamiltonian of the system can be given as

$$H = -J_1\sum_{ij}\sigma_i^z\sigma_j^z - J_s\sum_{m,i}S_m^z\sigma_i^z - J\sum_{n,i}S_n^z\sigma_i^z - D\sum_m(S_m^z)^2 - D_1\sum_i(\sigma_i^z)^2 - h(t)\sum_{m,i}(S_m^z + \sigma_i^z), \quad (1)$$

where $\sigma_i^z$ and $S_m^z$ represent spins $\pm 3/2$ and $\pm 2$, respectively. The anisotropies are expressed as $D_1$ and $D$, respectively, and $h(t)$ is the magnetic field, which is composed of time-dependent oscillating and time-independent magnetic fields. To simplify the calculation, in the following calculation process, $J_1 = 1$ is taken as the unit. Therefore, $h(t)$ is written as

$$h(t) = h_{\rm bias} + h_{\rm osc}\sin(2\pi^* t/\tau), \quad (2)$$

where $h_{\rm bias}$ denotes the value of the bias field, $h_{\rm osc}$ and $\tau$ represent the amplitude and period of the time-dependent oscillating field, respectively, and $t$ represents the time measured by the MC simulation per spin step.

To simulate the magnetic properties of the Kagome model, we adopted the MC method based on the Metropolis algorithm [46]. To maintain the equilibrium of the system and ensure the reliability of the calculation results, we discarded the initial $3 \times 10^5$ MC steps per spin and calculated the magnetic and thermodynamic quantities using the remaining $2 \times 10^5$ MC steps. The system shown in figure 1 has 48 magnetic atoms divided into five sublattices ($N_1$, $N_2$, $N_3$, $N_4$, and $N_5$). Sublattice $A$ is composed of $N_1$ and $N_3$, and sublattice $A$ is composed of $N_2$, $N_4$, and $N_5$. The magnetizations per site are defined as

$$M_A = \frac{1}{N_A}\sum_{i=1}^{N_A} S_i^z,$$
$$M_B = \frac{1}{N_B}\sum_{j=1}^{N_B} \sigma_j^z, \quad (3)$$

where $N_A$ is the number of sites in sublattices $N_1$ and $N_3$, and $N_B$ represents the number of sites in sublattices $N_2$, $N_4$, and $N_5$. Therefore, we can evaluate the total magnetization of the system as

$$M = \frac{N_A M_A + N_B M_B}{N_A + N_B}. \quad (4)$$

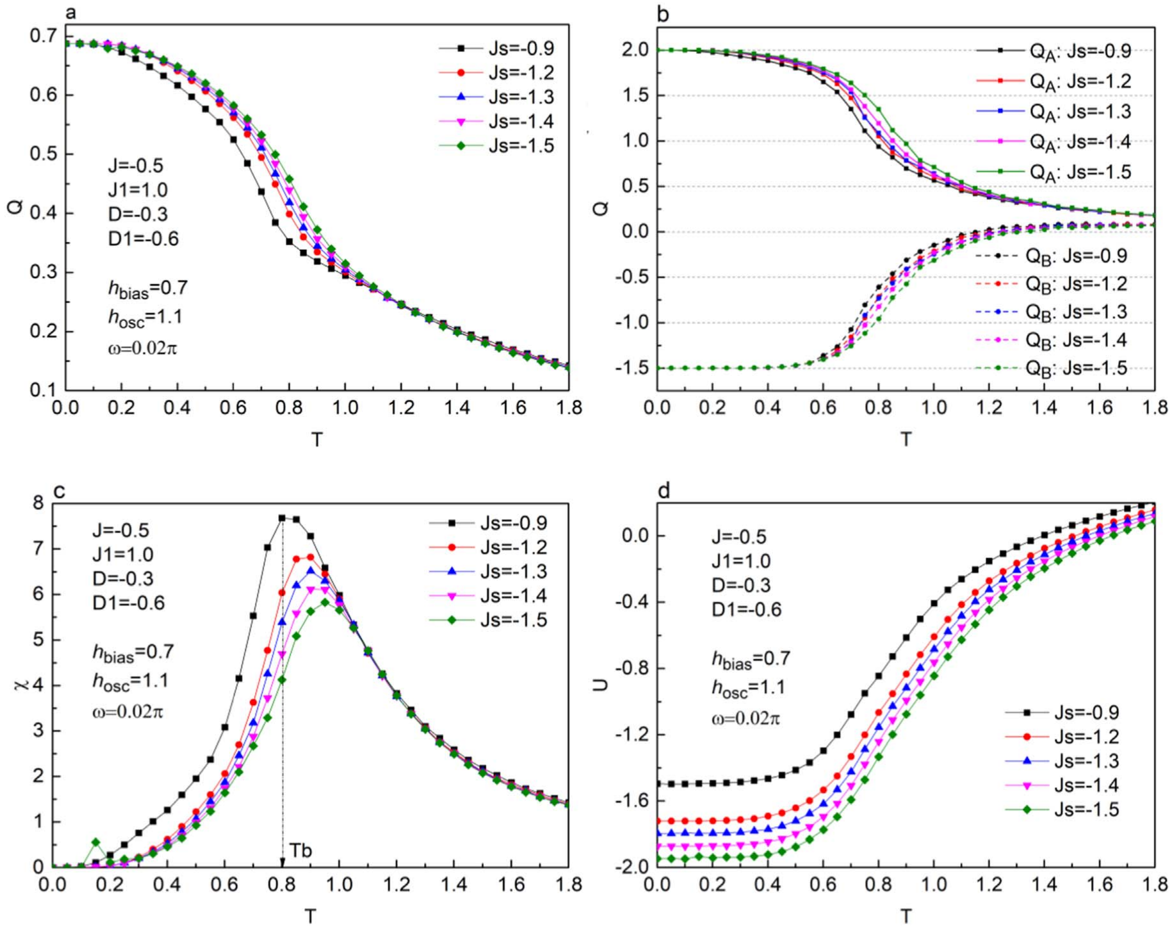

**Figure 3.** Temperature dependence of (a) the total dynamic order parameter $Q$, (b) dynamic order parameters $Q_A$ and $Q_B$, (c) susceptibility $\chi$, and (d) the internal energy $U$ for various $J_s$ with $J=-0.5$, $J_1=1.0$, $D=-0.3$, $D_1=-0.6$, $h_{\text{bias}}=0.7$, $h_{\text{osc}}=1.1$ and $\omega=0.02\pi$.

The dynamic order parameters of the five sublattices are expressed as

$$Q_A=\frac{\omega}{2\pi}\oint M_A(t)\mathrm{d}t,$$
$$Q_B=\frac{\omega}{2\pi}\oint M_B(t)\mathrm{d}t. \tag{5}$$

The dynamic order parameter is calculated as

$$Q=\frac{Q_AN_A+Q_BN_B}{N_A+N_B}\quad(N=48). \tag{6}$$

We defined dynamic magnetic susceptibility as

$$\chi=\frac{N}{k_{\mathrm{B}}T}(\langle Q^2\rangle-\langle Q\rangle^2). \tag{7}$$

The instantaneous internal energy per spin is calculated using

$$E(t)=\frac{1}{2N^2}\langle H\rangle. \tag{8}$$

We can calculate the dynamical internal energy per spin as follows:

$$U=\frac{\omega}{2\pi}\oint E(t), \tag{9}$$

where $k_{\mathrm{B}}$ represents the Boltzmann constant, which we set to 1. The magnetic entropy of the system is calculated as follows:

$$S(T,h)=\int_{T_0}^{T}\frac{C(T,h)}{T}\mathrm{d}T. \tag{10}$$

The magnetic entropy change can be expressed as

$$\Delta S(T,h)=S(T,h)-S(T,0). \tag{11}$$

For a magnetocaloric material, the relative cooling power (RCP) is an important factor and is given by

$$\mathrm{RCP}=\int_{T_C}^{T_V}\Delta S_m(T)\mathrm{d}T. \tag{12}$$

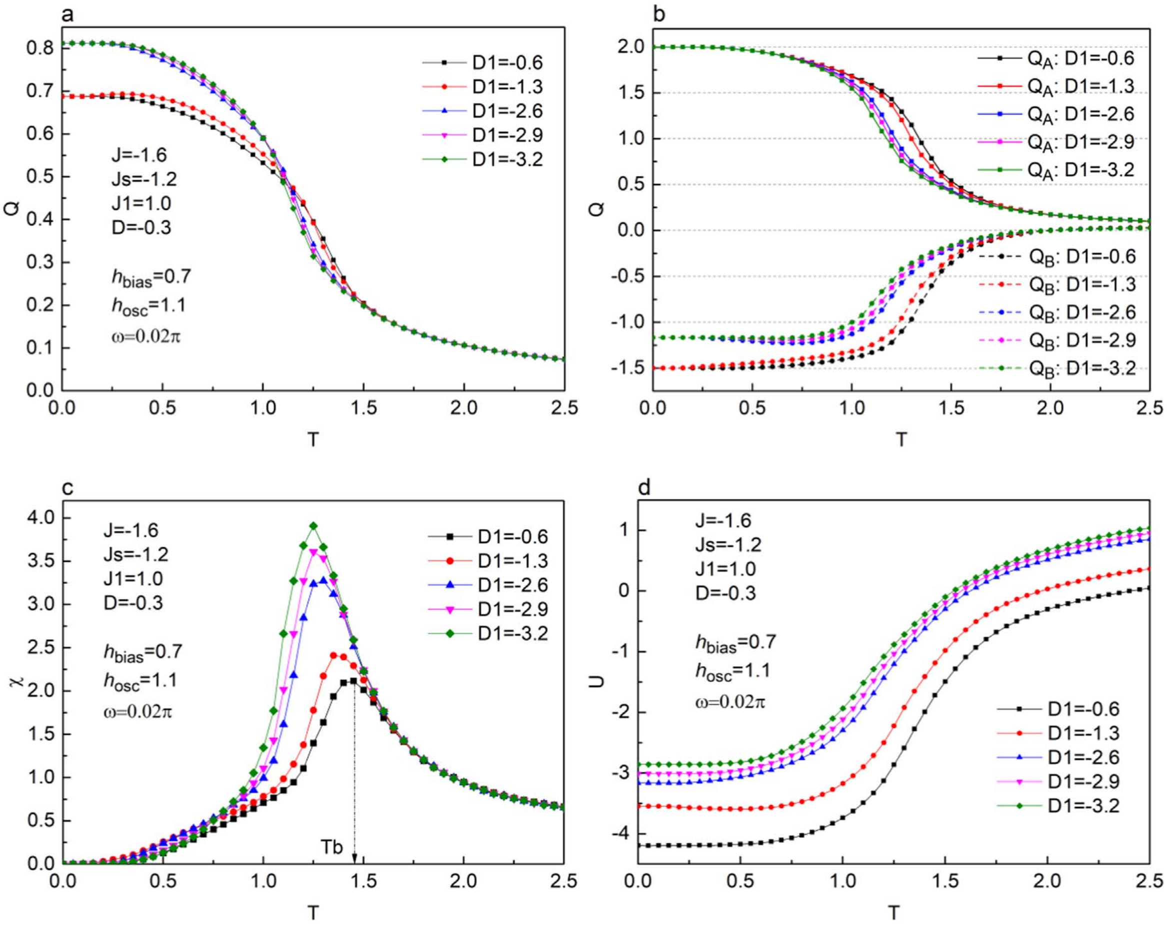

**Figure 4.** Temperature dependence of (a) the total dynamic order parameter $Q$, (b) dynamic order parameters $Q_A$ and $Q_B$, (c) susceptibility $\chi$, and (d) the internal energy $U$ for various $D_1$ with $J = -1.6$, $J_s = -1.2$, $J_1 = 1.0$, $D = -0.3$, $h_{\text{bias}} = 0.7$, $h_{\text{osc}} = 1.1$, and $\omega = 0.02\pi$.

The temperatures at either end of the half-maximum value of $\Delta S_{\max}$ are $T_c$ and $T_v$, respectively.

## 3. Results and discussion

We demonstrated the influences of diverse parameters on dynamic thermodynamic quantities, such as $Q$, $Q_A$, $Q_B$, $\chi$, and $U$ on the Kagome lattice.

### 3.1. Dynamic order parameter, susceptibility, and internal energy

Figure 2 shows the variations in the dynamic order parameters of the system when the exchange-coupling $J$ changes, and the remaining parameters are set to $J_s = -1.2$, $J_1 = 1.0$, $h_{\text{bias}} = 0.7$, $h_{\text{osc}} = 1.1$, $D = -0.3$, $D_1 = -0.6$, and $\omega = 0.02\pi$. Figure 2(a) shows the functional relationship between the average total dynamic order parameters ($Q$) and temperature ($T$) for different values of $J$. Only one saturation value ($Q_s = 11/16$) exists on all the $Q - T$ curves. The curves begin at this value and then gradually decline to a constant value. The effects of $J$ on $Q$ are not obvious when $T < 0.25$ or $T > 0.75$. When $0.25 < T < 0.75$, $Q$ increases slowly with the increase in $J$. Moreover, for a certain $T$, the higher the $J$, the higher the $Q$, which indicates that strong exchange coupling accelerates the order energy of the system. From figure 2(b), the saturation values of $Q_A$ and $Q_B$ at $T = 0$, $Q_A = 2.0$, and $Q_B = -1.5$, can be observed. Therefore, $Q_S = (30 \times 2 + 18 \times (-3/2))/48 = 11/16$. Furthermore, $Q_A$ and $|Q_B|$ decrease with the increase in $T$, whereas $Q_A$ and $|Q_B|$ increase with the decrease in $J$, indicating that a high $T$ or small $J$ facilitates a disordered system. As shown in figure 2(c), every $\chi - Q$ curve has a maximum, which corresponds to the blocking temperature $T_b$, where $T_b$ is a physical quantity that depends on ferromagnetic and antiferromagnetic (ferrimagnetic) materials. The system is in the ferromagnetic (ferrimagnetic) phase when $T < T_b$ and in the paramagnetic phase when $T > T_b$. As $T$ increases, the $\chi$ curves gradually shift to the high-temperature region. This behavior can be explained by an increase in the order energy of the system owing to the increase in $J$. Therefore, an increased amount of thermal energy is required to bring the system to disorder. In figure 2(d), the $U$ curves are observed to increase as $T$ increases and maintain a similar change rule. More specifically, when the temperature is low, $U$ maintains a constant value. With the increase in $T$, $U$ increases rapidly and subsequently slows. In addition, we observe that for the same temperature, $U$ decreases as $|J|$ increases.

Figure 3 shows the dynamic thermodynamic variables of the system when $J_s$ changes and the other parameters are fixed

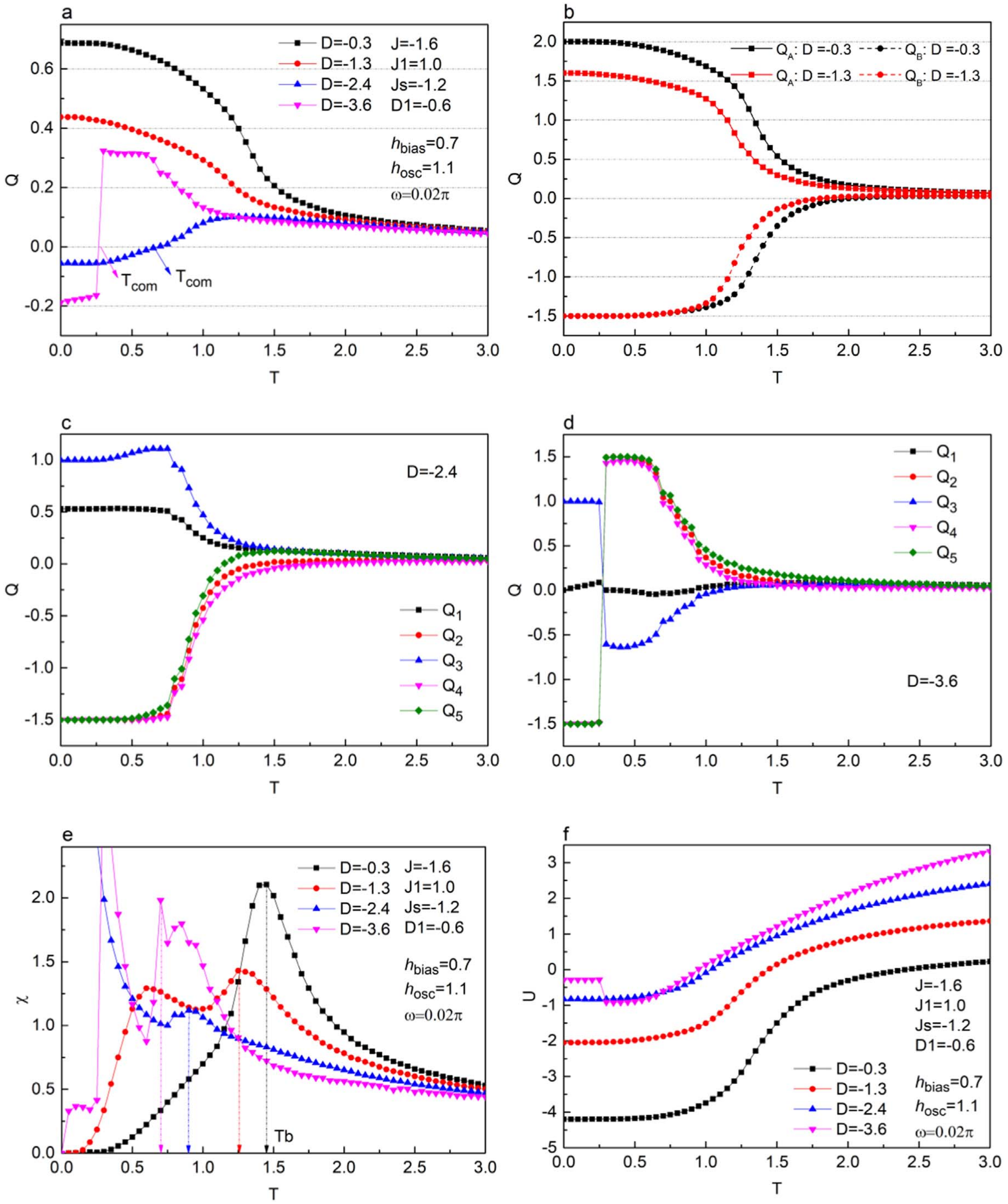

**Figure 5.** Temperature dependence of (a) the total dynamic order parameter $Q$, (b) dynamic order parameters $Q_A$ and $Q_B$ at $D = -0.3$ and $D = -1.3$, (c) dynamic order parameters of the five sublattices at $D = -2.4$, (d) dynamic order parameter of the five sublattices at $D = -3.6$, (e) susceptibility $\chi$, and (f) internal energy $U$ for various $D$ with $J = -1.6$, $J_s = -1.2$, $J_1 = 1.0$, $D_1 = -0.6$, $h_{\mathrm{bias}} = 0.7$, $h_{\mathrm{osc}} = 1.1$, and $\omega = 0.02\pi$.

at $J = -0.5$, $J_1 = 1.0$, $h_{\mathrm{bias}} = 0.7$, $h_{\mathrm{osc}} = 1.1$, $D = -0.3$, $D_1 = -0.6$, and $\omega = 0.02\pi$. As shown in figure 3(a), the $Q-T$ curves show a similar trend; they all start from the saturation value ($Q_s = 11/16$) at zero temperature. With an increase in temperature, the curve of $Q$ shows a rapid decline and finally converges to a steady value. As shown in figure 3(b), both $Q_A$ and $Q_B$ curves shift to the right with the increase in $J_s$; this phenomenon is similar to that shown in figure 2(b). From figure 3(c), we can clearly see that $T_b$ increases with an increase in $J_s$. This is similar to the influence of $J$ on the system; however, $J_s$ has a smaller influence on the $T_b$ of the system than that of $J$, as seen from the susceptibility curve obtained from changing $J$. This is because the changes in $J_s$ only influence the spin states of the peripheral sublattice, and the number of atoms in the periphery is relatively small. Figure 3(d) shows that with an increase in temperature, the $U$

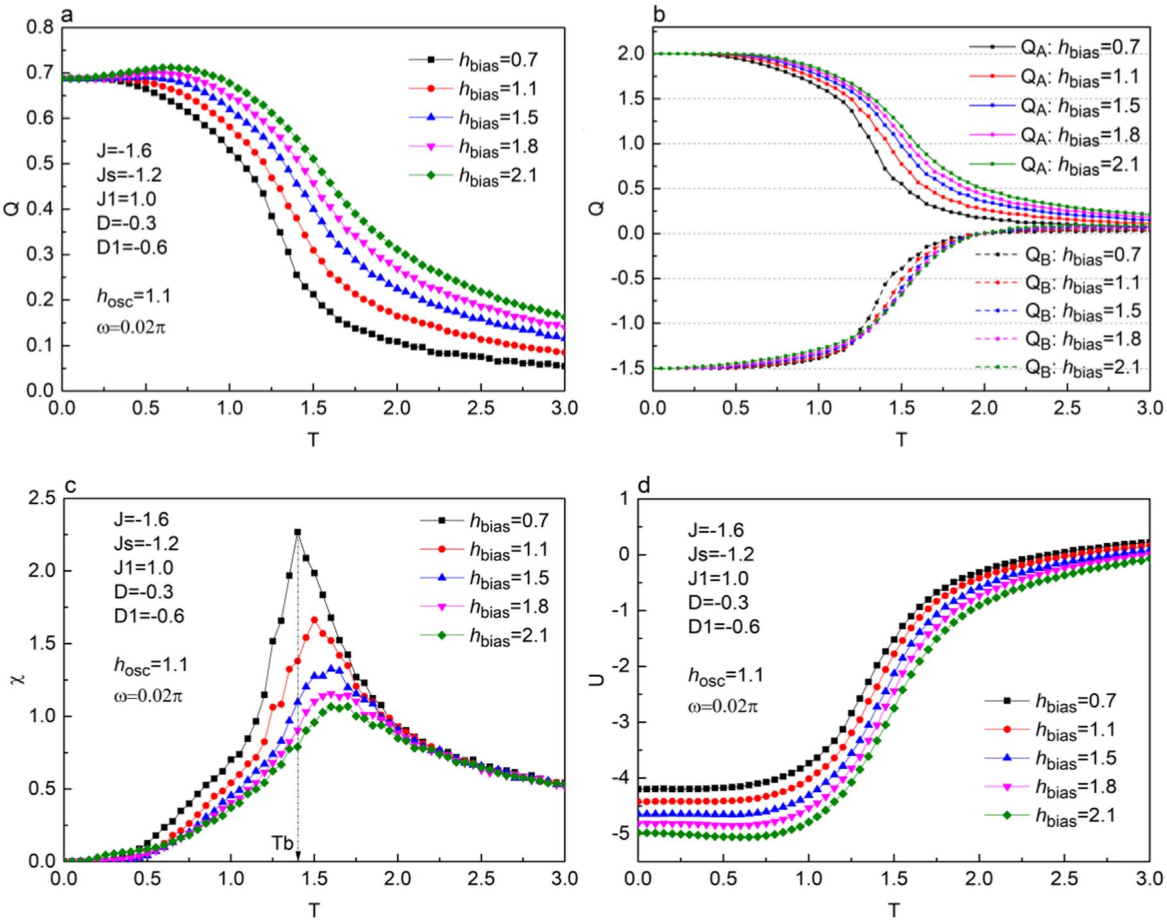

**Figure 6.** Temperature dependence of (a) the total dynamic order parameter $Q$, (b) dynamic order parameters $Q_A$ and $Q_B$, (c) susceptibility $\chi$, and (d) internal energy $U$ for different $h_{\text{bias}}$ at $J = -1.6$, $J_s = -1.2$, $J_1 = 1.0$, $D = -0.3$, $D_1 = -0.6$, $h_{\text{osc}} = 1.1$, and $\omega = 0.02\pi$.

curves start to increase and finally stabilize. Each $U$ curve reaches an inflection point corresponding to $T_b$, after which the positive slope of the curve starts to decrease, and the variation law of the curve is similar to that observed in figure 2(d).

In figure 4, we show $Q$, $Q_A$, $Q_B$, $\chi$, and $U$ as functions of temperature for different values of $D_1$ with the fixed values $J = -1.6$, $J_s = -1.2$, $J_1 = 1.0$, $h_{\text{bias}} = 0.7$, $h_{\text{osc}} = 1.1$, $D = -0.3$, and $\omega$=0.02$\pi$. Two saturation values ($Q = 11/16$ and $13/16$) appear on the $Q$ curves, as shown in figure 4(a). In addition, $Q$ decreases from the saturation value as the temperature increases with the increase in $T$ and eventually approaches a non-zero value because of the magnetic field used as an external bias. In figure 4(b), two saturation values are observed: $Q_B = -3/2$ and $-7/6$. However, $Q_A$ has a common saturation value $Q_A$ of 2.0. Furthermore, $Q_A$ and $Q_B$ together saturate the $Q$ in figure 4(a), i.e. $Q = [(2 \times 30) + ((-3/2) \times 18)]/48 = 11/16$, $Q = [(2 \times 30) + ((-7/6) \times 18)]/48 = 13/16$ using equation (5). From figure 4(c), we observe that with an increase in $|D_1|$, the corresponding $T_b$ decreases. This is because strong anisotropy changes the system from a high-spin state to a low-spin state. Therefore, with an increase in $|D_1|$, less heat energy is required to break the magnetic order. As shown in figure 4(d), with an increase in $|D_1|$, the $U$ of the system increases. In the low- and high-temperature regions, the value of $U$ increases slowly and rapidly, respectively. This is because each lattice is significantly affected by anisotropy at low temperatures, but the thermal disturbance energy gradually becomes dominant with an increase in temperature. In addition, when the temperature is fixed, the larger the $|D_1|$, the larger the $U$ of the system.

Figure 5 clearly shows the effect of anisotropy $D$ on $Q$, $\chi$, and $U$ for $J = -1.6$, $J_s = -1.2$, $h_{\text{bias}} = 0.7$, $h_{\text{osc}} = 1.1$, $D_1 = -0.6$, and $\omega = 0.02\pi$. In figure 5(a), four saturation values of $Q$, i.e. $11/16$, $7/16$, $-11/20$, and $-3/16$, at $T = 0$ are displayed at $D = -0.3$, $-1.3$, $-2.4$, and $-3.6$, respectively. For instance, when $D = -0.3$, figure 5(b) shows that the saturation values of the two sublattices are $Q_A = 2.0$ and $Q_B = -1.5$, respectively. Therefore, the saturation value of the system is $Q_s = 11/16$. When $|D|$ increases to 1.3, $Q_A$ decreases and $Q_B$ remains unchanged. A strong anisotropy can maintain the spin of sublattice A at a low state. Figures 5(c) and (d) show the dynamic order parameters of the five sublattices when $D = -2.4$ and $-3.6$, respectively. At $T = 0$, $Q_2 = Q_4 = Q_5 = -1.5$ and $Q_3 = 1.0$. However, as $D$ decreases from $-2.4$ to $-3.6$, the saturation value of $Q_1$ changes, i.e. $Q_1 = 13/25$ at $D = -2.4$ and $Q_1 = 0$ at $D = -3.6$. A more interesting phenomenon is observed when $|D| = 3.6$; the $Q_2$, $Q_3$, $Q_4$, $Q_5$ curves of the sublattices change

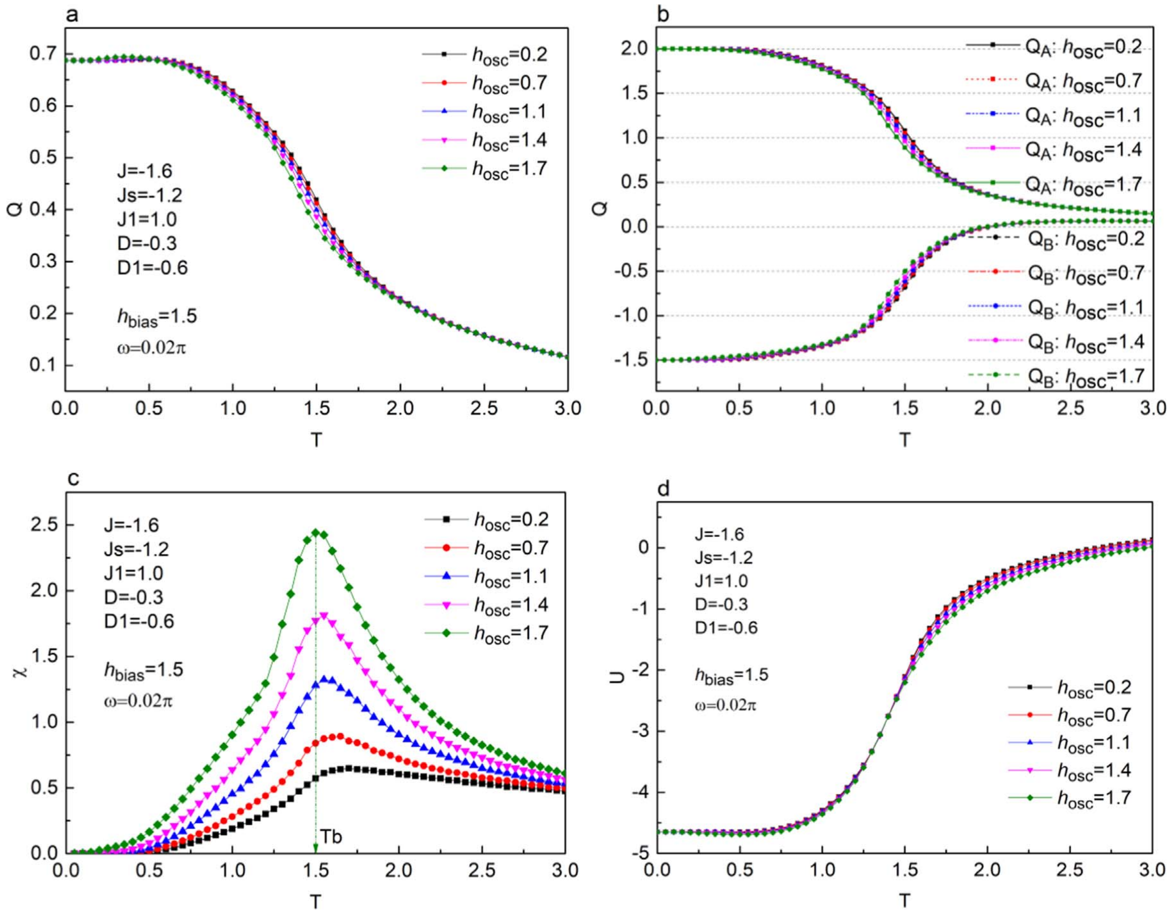

**Figure 7.** Temperature dependence of (a) the total dynamic order parameter $Q$, (b) dynamic order parameters $Q_A$ and $Q_B$, (c) susceptibility $\chi$, and (d) internal energy $U$ for various $h_{\mathrm{osc}}$ at $J=-1.6$, $J_s=-1.2$, $J_1=1.0$, $D=-0.3$, $D_1=-0.6$, $h_{\mathrm{bias}}=1.5$, and $\omega=0.02\pi$.

to the opposite direction with increasing $T$. Notably, when $D=-2.4$, the saturation value of $13/25$ for $Q_1$ is owing to the sublattices not responding to the magnetic field simultaneously, causing the change in direction. The directions of the $Q$ curves labeled $-2.4$ and $-3.6$ in figure 5(a) change from negative to positive at a certain $T$. When the magnetization is zero, the corresponding temperature is called the compensation temperature $T_{\mathrm{com}}$, which decreases with increasing $|D|$. As shown in figure 5(e), $T_b$ increases as $|D|$ decreases. In addition, double peaks are observed on the $\chi$ curve owing to thermal agitation. From figure 5(f), as both $T$ and $|D|$ increase, $U$ increases. In addition, in the low-temperature zone, a noticeable fluctuation is observed for $D=-3.6$, where $U$ decreases and then increases. This behavior is related to the changing directions of the $Q$ curves.

The temperature dependencies of $Q$, $Q_A$, $Q_B$, $\chi$, and $U$ for different values of $h_{\mathrm{bias}}$ at $J=-1.6$, $J_s=-1.2$, $J_1=1.0$, $D=-0.3$, $D_1=-0.6$, $h_{\mathrm{osc}}=1.1$, and $\omega=0.02\pi$, are shown in figure 6. As shown in figure 6(a), all $Q$ curves have the same saturation value ($Q_s=11/16$). When $h_{\mathrm{bias}}$ is relatively small ($h_{\mathrm{bias}}=0.7$, 1.2, or 1.5), the $Q$ curves decrease monotonously with increasing $T$. When $h_{\mathrm{bias}}$ is large ($h_{\mathrm{bias}}=1.8$, or 2.1), the $Q$ curves first increase and then decrease with an increase in $T$. We observed that the $Q-T$ curves do not converge to the same value; a high $h_{\mathrm{bias}}$ leads to a high convergence value of $Q$. This reveals that the bias field has a significant impact on the dynamic order parameters at high temperatures. In figure 6(b), the saturation values of $Q_A$ and $Q_B$ are observed to be 2.0 and $-1.5$, respectively. When $T<1.0$, the bias field $h_{\mathrm{bias}}$ has little effect on $Q_A$ and $Q_B$. However, when $T>1.0$, with the increase in $h_{\mathrm{bias}}$, the values of $Q_A$ and $Q_B$ decrease significantly. Figure 6(c) shows that $T_b$ increases as $h_{\mathrm{bias}}$ increases. This is because an increase in $h_{\mathrm{bias}}$ indicates that the magnetic ordering energy of the system increases. Therefore, breaking the order of the system requires more thermal energy to achieve a dynamic paramagnetic phase. In figure 6(d), $U$ is observed to increase with an increase in $T$ but decreases with an increase in the bias field $h_{\mathrm{bias}}$.

Figure 7 shows the effect of $h_{\mathrm{osc}}$ on $Q$, $Q_A$, $Q_B$, $\chi$, and $U$ at $J=-1.6$, $J_s=-1.2$, $J_1=1.0$, $D=-0.3$, $D_1=-0.6$, $h_{\mathrm{bias}}=1.5$, and $\omega=0.02\pi$. As seen in figure 7(a), all $Q$ curves have the same saturation value ($Q_s=11/16$). In the low- ($0<T<0.75$) and high-temperature ($1.75<T<2.5$) regions, $Q$ is not sensitive to $T$, whereas in the medium-temperature region ($0.75\leqslant T\leqslant 1.75$), $T$ becomes the dominant factor affecting $Q$. We observe that for the same $T$, the value of $Q$ decreases as $h_{\mathrm{osc}}$ increases. As shown in figure 7(b), when the value of $h_{\mathrm{osc}}$ increases, the values of $Q_A$ and $Q_B$ gradually decrease. Figure 7(c) reveals that as $h_{\mathrm{osc}}$ increases, $T_b$ shifts towards the low-temperature region. The

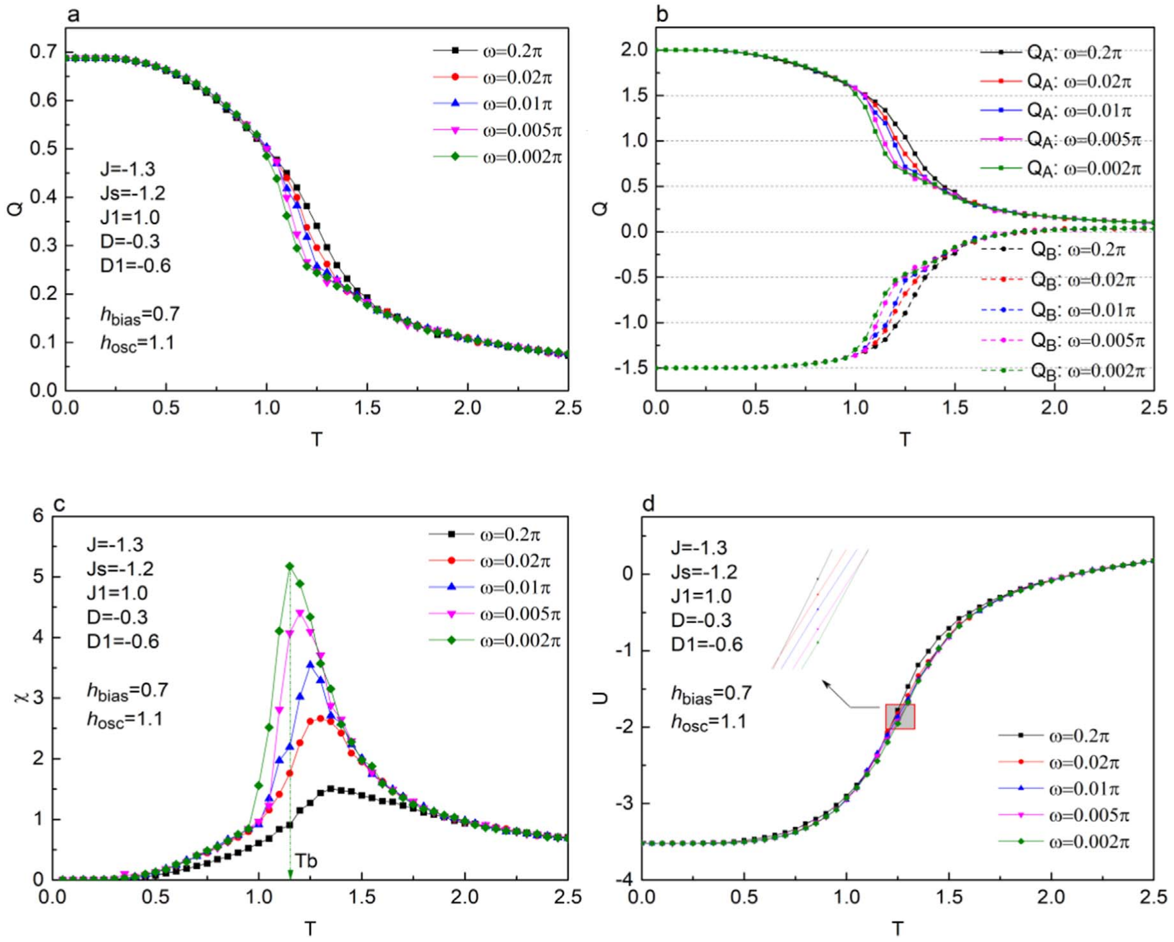

**Figure 8.** Temperature dependence of (a) the total dynamic order parameter $Q$, (b) dynamic order parameters $Q_A$ and $Q_B$, (c) susceptibility $\chi$, and (d) internal energy $U$ for different $\omega$ at $J=-1.3$, $J_s=-1.2$, $J_1=1.0$, $D=-0.3$, $D_1=-0.6$, $h_{\text{bias}}=0.7$, $h_{\text{osc}}=1.1$.

reason for this phenomenon is that when the other parameters are constant, increasing the amplitude of the external magnetic field that is oscillating is equivalent to increasing the disordered energy of the system; thereby reducing the energy required for the system to break the ordered state of the system. Figure 7(d) shows that in the high-temperature region, $T$, instead of $h_{\text{osc}}$, dominates the influence of internal energy.

The effect of $\omega$ on $Q$, $Q_A$, $Q_B$, $\chi$, and $U$ at $J=-1.3$, $J_s=-1.2$, $D=-0.3$, $D_1=-0.6$, $h_{\text{bias}}=0.7$, and $h_{\text{osc}}=1.1$ is shown in figure 8. In figure 8(a), unlike the other $Q$-curves (for example, those in figure 2(a)), when $T<1.0$ or $T>1.5$, $Q$ is insensitive to the changes in $\omega$. When $1.0\leqslant T\leqslant 1.5$, the value of $Q$ increases as $\omega$ increases. This is because, in the case of low or high temperatures, the influence of temperature on the total dynamic order parameters is the main factor. Figure 8(b) shows that both $Q_A$ and $|Q_B|$ decrease as $\omega$ decreases and as the temperature increases. Notably, in figure 8(c), $T_b$ increases with the increase in $\omega$; $\omega$ represents the frequency of the magnetic field oscillation. When $\omega$ is small, the magnetic field oscillates slowly and the spin directions of the sublattices can easily follow the change in the time-dependent oscillating magnetic field, which indicates that the system requires less thermal energy to become disordered. The increased $\omega$ causes the dynamic order parameter to not respond instantaneously to the oscillating magnetic field, thereby requiring more thermal energy for phase transition. In figure 8(d), we identify that when $T$ is fixed, $U$ increases as $\omega$ increases after local amplification. For the same $\omega$, the value of $U$ increases at high values of $T$.

### 3.2. Phase diagram

To further clarify the effect of various parameters on the blocking temperature, we sorted the results of $T_b$ under the influence of different parameters and plotted the corresponding phase diagrams in figures 9(a)–(f). Figures 9(a)–(b) show the effects of $J$ and $J_s$ on $T_b$ with the other parameters set as $h_{\text{bias}}=0.7$, $h_{\text{osc}}=1.1$, $D=-0.3$, $D_1=-0.6$, and $\omega=0.02\pi$. Additionally, $T_b$ increases monotonically with increasing $|J|$ and $|J_s|$. This is owing to the increase in exchange coupling that essentially increases the interaction forces of the magnetic sublattices in the system, thereby increasing the ordering energy of the system. Therefore, a large $T_b$ is required for the phase transition of the system. In addition, the change in $J_s$ has a smaller effect on $T_b$ compared with that of $J$, because $J$ controls more of the sublattices than $J_s$. Figures 9(c)–(d) show the effect of $D$ and $D_1$ on $T_b$ with other parameters fixed at $J=-1.6$, $J_s=-1.2$, $J_1=1.0$, $h_{\text{bias}}$

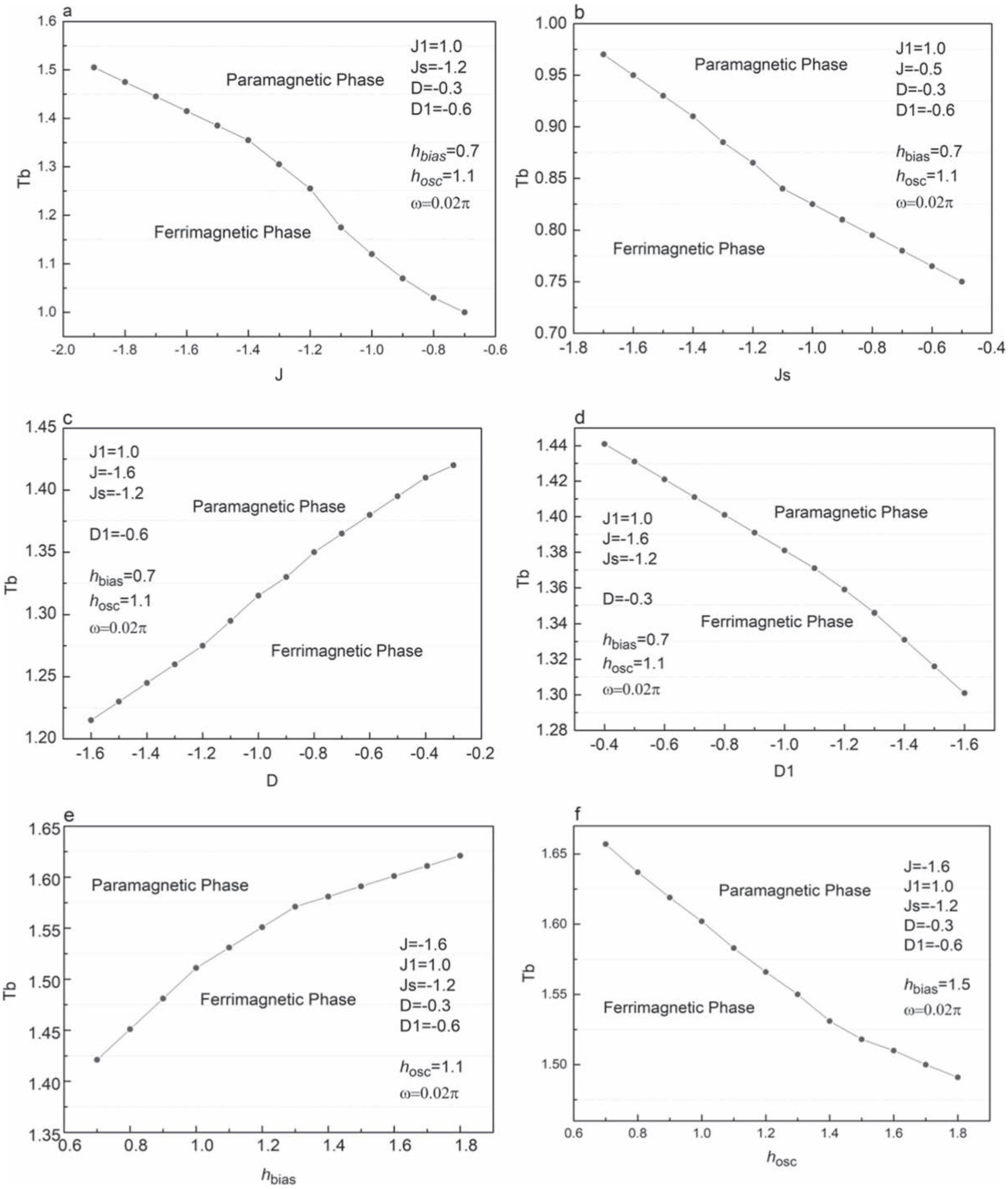

**Figure 9.** Phase diagrams of $T_b$ (a) in the ($J$, $T$) plane with $h_{\rm bias} = 0.7$, $h_{\rm osc} = 1.1$, $J_s = -1.2$, $D = -0.3$, $D_1 = -0.6$, and $\omega = 0.02\pi$; (b) ($J_s$, $T$) plane $h_{\rm bias} = 0.7$, $h_{\rm osc} = 1.1$, $J = -0.5$, $D = -0.3$, $D_1 = -0.6$, and $\omega = 0.02\pi$; (c) ($D$, $T$) plane with $J = -1.6$, $J_s = -1.2$, $D_1 = -0.6$, $h_{\rm bias} = 0.7$, $h_{\rm osc} = 1.1$, and $\omega = 0.02\pi$; (d) ($D_1$, $T$) plane with $J = -1.6$, $J_s = -1.2$, $D = -0.3$, $h_{\rm bias} = 0.7$, $h_{\rm osc} = 1.1$, and $\omega = 0.02\pi$; (e) ($h_{\rm bias}$, $T$) plane $J = -1.6$, $J_s = -1.2$, $D = -0.3$, $D_1 = -0.6$, $h_{\rm osc} = 1.1$, and $\omega = 0.02\pi$; (f) ($h_{\rm osc}$, $T$) plane with $J = -1.6$, $J_s = -1.2$, $D = -0.3$, $D_1 = -0.6$, $h_{\rm bias} = 1.5$, and $\omega = 0.02\pi$.

$= 0.7$, $h_{\rm osc} = 1.1$, and $\omega = 0.02\pi$. Additionally, as $D$ and $|D_1|$ increase, $T_b$ decreases, which indicates that a large anisotropy is not conducive to the order of the system. Moreover, the change in $D_1$ affects $T_b$ less than the changes in $D$, owing to the reduced number of sublattices with anisotropy $D_1$. Figures 9(e)–(f) show the effect of $h_{\rm bias}$ and $h_{\rm osc}$ on $T_b$ with other parameters fixed at $J = -1.6$, $J_s = -1.2$, $J_1 = 1.0$, $D = -0.3$, $D_1 = -0.6$, and $\omega = 0.02\pi$. Furthermore, $T_b$ increases monotonically with increasing $h_{\rm bias}$ because $h_{\rm bias}$ improves the order of the system. In addition, $h_{\rm bias}$ and $h_{\rm osc}$ have opposite effects on $T_b$ because the increase in $h_{\rm osc}$ increases the disorder of the system.

### 3.3. Magnetocaloric effect

The magnetocaloric effect on the Kagome lattice was investigated. The temperature dependence of magnetization $M$ of the Kagome lattice is shown in figure 10. We observe that $M$

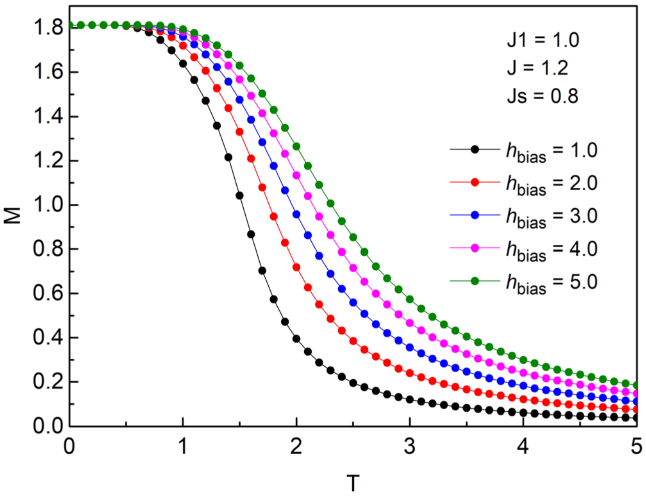

**Figure 10.** Magnetization as a function of $T$ for different $h_{\text{bias}}$.

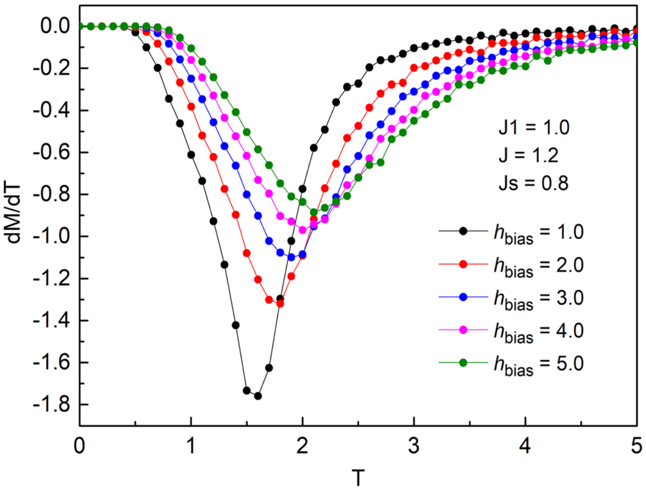

**Figure 11.** dM/dT as a function of $T$ for different $h_{\text{bias}}$.

starts at the saturation value ($M_s = 29/16$) at zero temperature and then decreases with increasing $T$. Figure 11 shows the thermal magnetizations ($\mathrm{d}M/\mathrm{d}T$) with different values of bias field $h_{\text{bias}}$. These curves indicate that at the critical temperature $T_c$, the magnetic transition changes from the ferromagnetic phase to the paramagnetic phase. The corresponding transition temperatures increase with increasing $h_{\text{bias}}$. For example, $T_c = 1.601$ for $h_{\text{bias}} = 1.0$ and $T_c = 2.101$ for $h_{\text{bias}} = 5.0$. We calculated the magnetic entropy using equation (11). Figure 12 shows the variation trend in the magnetic entropy $\Delta S$ of the Kagome lattice as a function of $T$ with different $h_{\text{bias}}$. A maximum value at the critical temperature can be seen in the $-\Delta S$ curves. This maximum value $-\Delta S_{\max}$ increases with increasing $h_{\text{bias}}$. For $h_{\text{bias}} = 1.0$, 2.0, 3.0, 4.0, and 5.0, $-\Delta S_{\max} = 1.759$, 2.639, 3.295, 3.880, and 4.426, respectively. In addition, figure 13 shows an interesting parameter for evaluating potential materials for magnetic refrigeration, i.e. RCP, which is a function of $h_{\text{bias}}$ for the Kagome lattice. Furthermore, RCP is found to increase linearly as $h_{\text{bias}}$ increases and reaches a value of 8.281 at $h_{\text{bias}} = 6.0$.

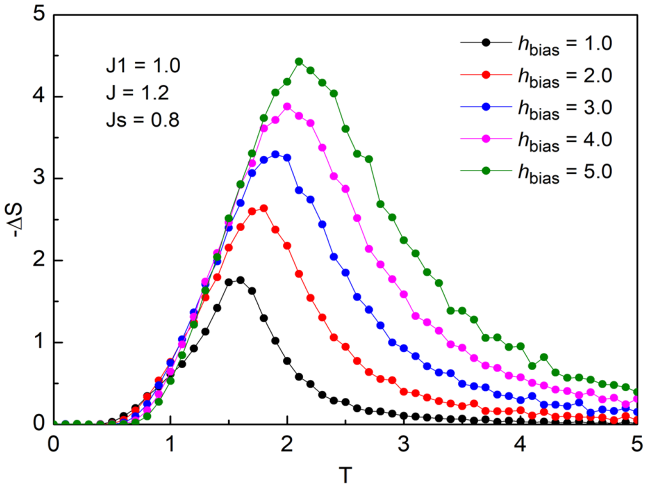

**Figure 12.** Temperature dependence of the entropy variation with different $h_{\text{bias}}$.

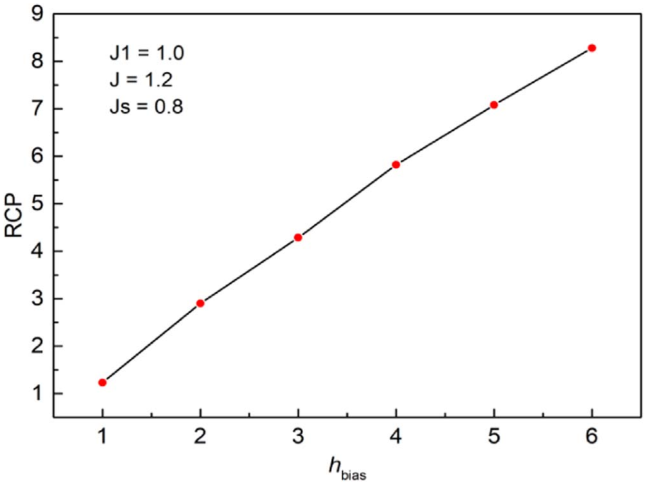

**Figure 13.** Bias field dependence of the RCP associated with the system for $J_1 = 1.0$, $J = 1.2$, and $J_s = 0.8$.

Figure 14 shows the dependence of $T$ on the $M$ of the system. The figure shows that all $M$ curves decrease from the saturation value ($M_s = 29/16$) to a steady-state value with increasing $T$. When $T$ is fixed, $M$ increases with increasing $J$. Figure 15 shows the ($\mathrm{d}M/\mathrm{d}T$) curves for different values of $J$. At $T_c$, the magnetic transition changes from the ferromagnetic phase to the paramagnetic phase. Furthermore, $T_c$ increases with increasing $J$, i.e. $T_c = 1.801$ for $J = 0.8$ and $T_c = 2.401$ for $J = 2.4$. Figure 16 shows the variation of $-\Delta S$ with the changes in temperature of the Kagome lattice for different values of $J$. The $-\Delta S$ curves reach a maximum value $-\Delta S_{\max}$ at $T_c$. This maximum value decreases with increasing $J$, i.e. for $J$ =0.8, 1.2, 1.6, 2.0, and 2.4, $-\Delta S_{\max} = 3.384$, 3.323, 3.169, 3.083, and 2.966, respectively. Figure 17 shows $J$ dependence of the RCP associated with the system. We found that RCP decreases linearly with increasing $J$.

Figure 18 shows the $M$ versus $T$ plots for different values of $J_s$ at $J = 1.2$, $J_1 = 1.0$, and $h_{\text{bias}} = 3.0$. Only one saturation value ($M_s = 29/16$) is shown in the figure. In figures 19 and 20, we additionally show ($\mathrm{d}M/\mathrm{d}T$) and $-\Delta S$ as

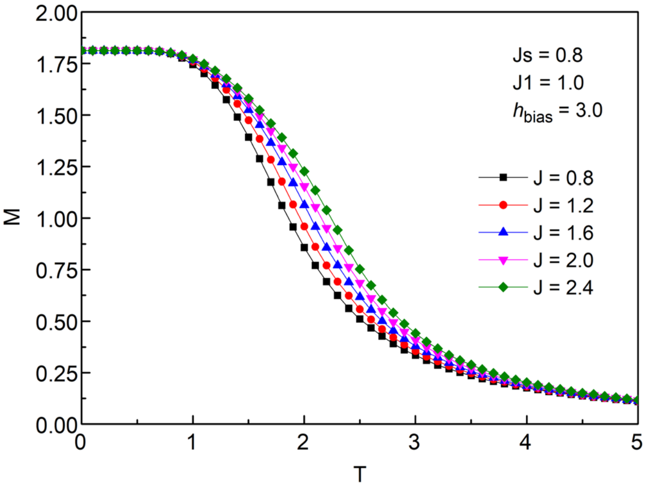

**Figure 14.** Magnetization as a function of $T$ for different $h_{\text{bias}}$.

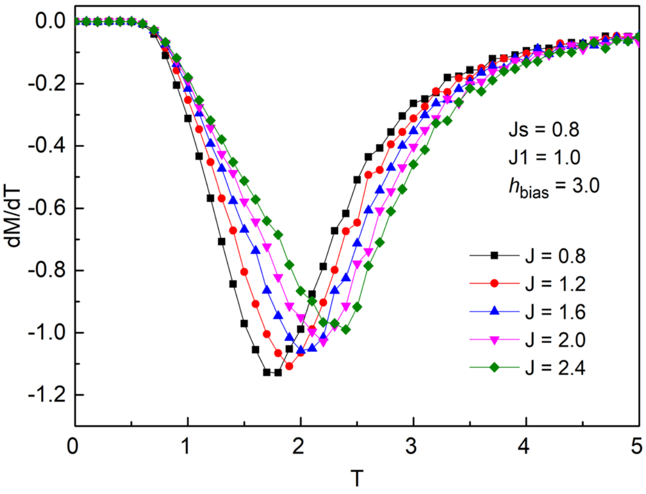

**Figure 15.** dM/dT as a function of $T$ for different $J$.

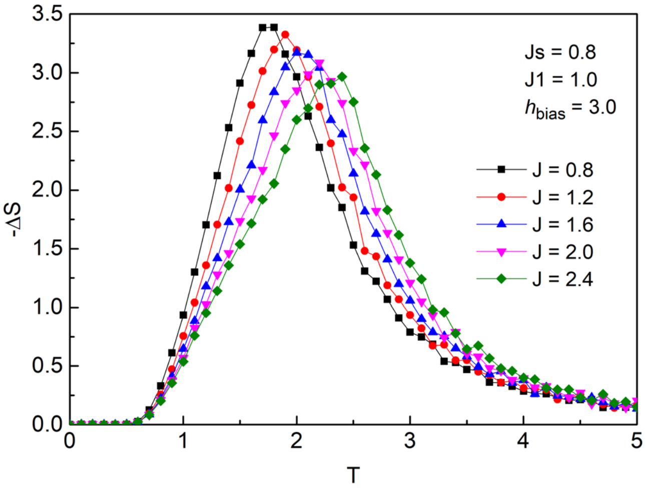

**Figure 16.** Temperature dependence of the entropy variation with different $J$.

a function of temperature with the same parameters as those in figure 19. The peaks corresponding to the $T_c$ of the system increase with increasing $J_s$. Figure 21 shows the exchange-coupling $J_s$ dependence of the RCP associated with the system. The RCP decreases with increasing $J_s$, similar to that in figure 17.

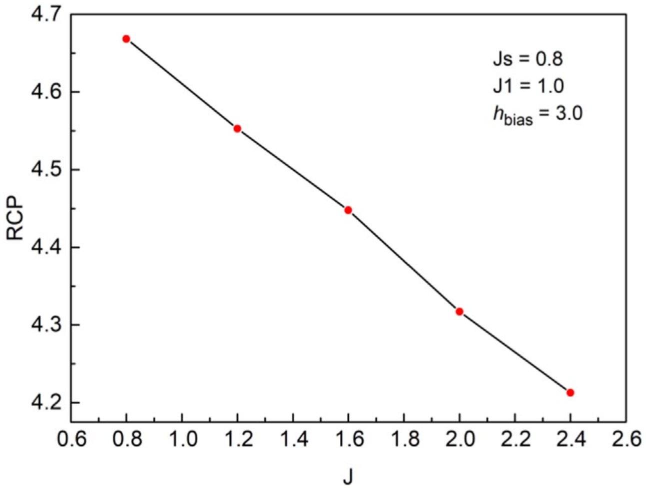

**Figure 17.** Exchange-coupling $J$ dependence of the RCP associated with the system at $h_{\text{bias}} = 3.0$, $J_s = 0.8$, and $J_1 = 1.0$.

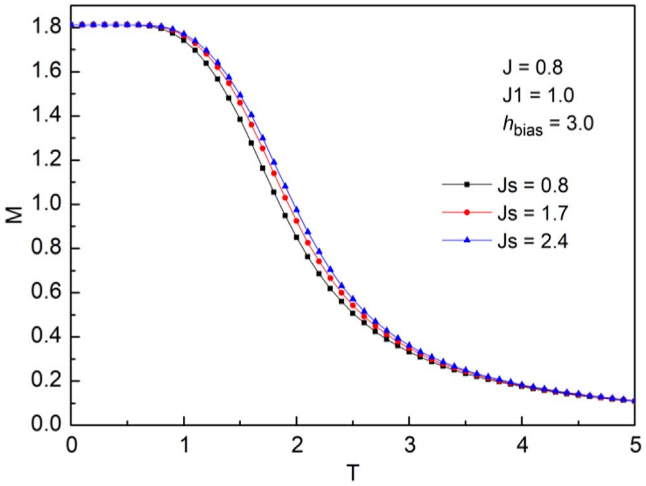

**Figure 18.** Magnetization as a function of $T$ for different $J_s$.

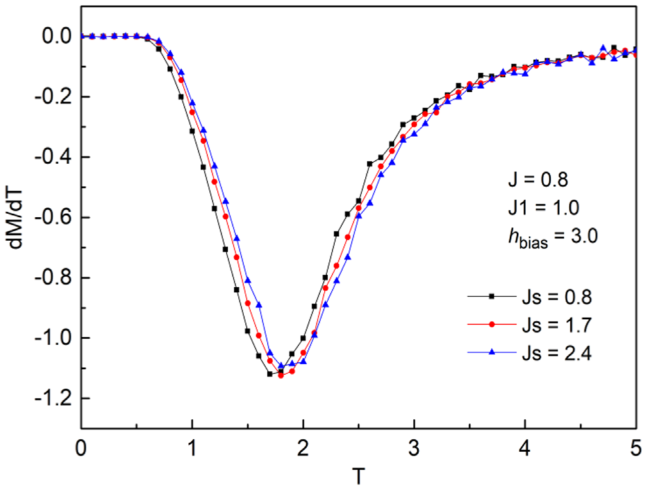

**Figure 19.** dM/dT as a function of $T$ for different $J_s$.

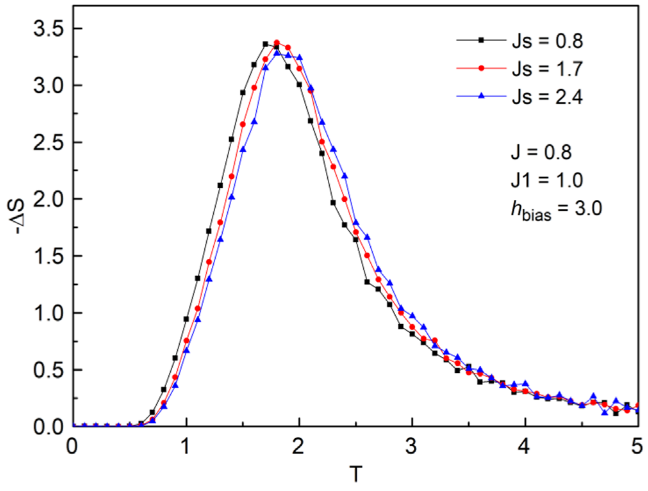

**Figure 20.** Temperature dependence of the entropy variation with different $J_s$.

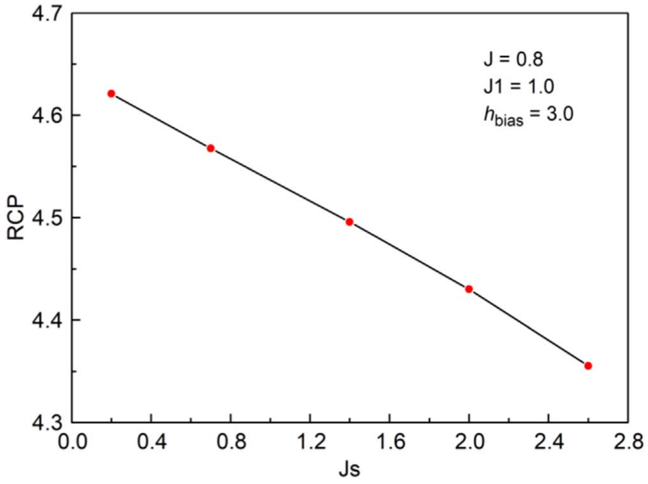

**Figure 21.** Exchange-coupling $J_s$ dependence of the RCP associated with the system at $h_{\text{bias}} = 3.0$, $J = 1.2$, and $J_1 = 1.0$.

## 4. Conclusions

In this study, we investigated the ferrimagnetic mixed-spin (2, 3/2) Kagome lattice using MC simulations. We discuss the effect of $J$, $J_s$, $D$, $D_1$, $h_{\text{bias}}$, $h_{\text{osc}}$, and $\omega$ on the dynamic phase transitions of the system. The system exhibits multiple spin flips when the system parameters are changed, and under certain parametric conditions, compensation point behavior is exhibited by the system. By analyzing the phase diagrams of $T_b$, we found that large $|J|$, $|J_s|$, $h_{\text{bias}}$, and $\omega$ values facilitate an increase in $T_b$; however, the increases in $D$, $D_1$, and $h_{\text{osc}}$ have the opposite effect on $T_b$. Moreover, $\Delta S$ as a function of $T$ for various $h_{\text{bias}}$ ($J$ and $J_s$) were also discussed. The RCP revealed that the magnetocaloric effect depends on the values of $h_{\text{bias}}$, $J$ and $J_s$.

## Acknowledgments

This project was supported by the Key project of the Education Department of Liaoning Province (Grant no. LJKZZ20220022) and the Key R&D project of Liaoning Province of China (Grant no. 2020JH2/10300079).

## References

[1] Mielke A 1992 Exact ground states for the Hubbard model on the Kagome lattice *J. Phys. A: Math. Gen.* **25** 4335
[2] Mielke A 1991 Ferromagnetic ground states for the Hubbard model on line graphs *J. Phys. A: Math. Gen.* **24** L73
[3] Mielke A 1991 Ferromagnetism in the Hubbard model on line graphs and further considerations *J. Phys. A: Math. Gen.* **24** 3311
[4] Tang E, Mei J W and Wen X G 2011 High-Temperature Fractional Quantum Hall States *Phys. Rev. Lett.* **106** 236802
[5] Wu C, Bergman D, Balents L and Das Sarma S 2007 Flat Bands and Wigner Crystallization in the Honeycomb Optical Lattice *Phys. Rev. Lett.* **99** 070401
[6] Huber S D and Altman E 2010 Bose condensation in flat bands *Phys. Rev.* B **82** 184502
[7] Wang Y F, Gu Z C, Gong C D and Sheng D N 2011 Fractional quantum hall effect of hard-core bosons in topological flat bands *Phys. Rev. Lett.* **107** 146803
[8] Sun K, Gu Z, Katsura H and Das Sarma S 2011 Nearly flatbands with nontrivial topology *Phys. Rev. Lett.* **106** 236803
[9] Imada M and Kohno M 2000 Superconductivity from Flat Dispersion Designed in Doped Mott Insulators *Phys. Rev. Lett.* **84** 143
[10] Peotta S and Törmä P 2015 Superfluidity in topologically nontrivial flat bands *Nat. Commun.* **6** 8944
[11] Sachdev S 1992 Kagome- and triangular-lattice Heisenberg antiferromagnets: Ordering from quantum fluctuations and quantum-disordered ground states with unconfined bosonic spinons *Phys. Rev.* B **45** 12377
[12] Balents L 2010 Spin liquids in frustrated magnets *Nature* **464** 199–208
[13] Yan S, Huse D A and White S R 2011 Spin-Liquid Ground State of the $S = 1/2$ Kagome Heisenberg Antiferromagnet *Science* **322** 1173–6
[14] Yoshida H, Noguchi N and Matsushita Y 2017 Unusual magnetic state with dual magnetic excitations in the single crystal of $S = 1/2$ kagome lattice antiferromagnet $CaCu_3(OH)_6Cl_2 - 0.6H_2O$ *J. Phys. Soc. Jpn.* **86** 033704
[15] Puphal P, Bolte M and Sheptyakov D 2017 Strong magnetic frustration in $Y_3Cu_9(OH)_{19}Cl_8$: a distorted kagome antiferromagnet *J. Mater. Chem.* C **5** 2629
[16] Sun W, Huang Y X and Nokhrin S 2016 Perfect Kagomé lattices in $YCu_3(OH)_6Cl_3$: a new candidate for the quantum spin liquid state *J. Mater. Chem.* C **4** 8772–7
[17] Szymczak R, Aleshkevych P and Adams C P 2009 Magnetic anisotropy in geometrically frustrated kagome staircase lattices *J. Magn. Magn. Mater.* **321** 793–5
[18] Jiang J H, Zhu B, Zhu T Y and Yang H M 2020 Open-framework ammonium transition metal fluorophosphates with a Kagomé lattice network: synthesis, structure and magnetic properties *Dalton T.* **49** 841–9
[19] Lin Z, Choi J H and Zhang Q 2018 Flatbands and emergent ferromagnetic ordering in $Fe_3Sn_2$ kagome lattices *Phys. Rev. Lett.* **121** 096401
[20] Si N, Su X and Meng J 2020 Magnetic properties of decorated 2D kagome-like lattice *Physica* A **560** 125222
[21] Ananikian N S, Ananikian L N and Lazaryan H A 2012 Magnetic properties and concurrence for fluid $^3$He on kagome lattice *Phys. Atom. Nucl.* **75** 1250–5

[22] Yerzhakov H V, Plumer M L and Whitehead J P 2016 Monte Carlo simulations of abc stacked kagome lattice films *J. Phys.: Condens. Matter* **28** 196003

[23] Soldatov K, Peretyatko A and Andriushchenko P 2019 Comparison of diluted antiferromagnetic Ising models on frustrated lattices in a magnetic field *Phys. Lett.* A **383** 1229–34

[24] Zhang Z D 2007 Conjectures on the exact solution of three-dimensional (3D) simple orthorhombic Ising lattices *Philos. Mag.* **87** 5309–419

[25] Zhang Z D 2013 Mathematical structure of the three-dimensional (3D) Ising model *Chinese Phys.* B **22** 030513

[26] Zhang Z D, Suzuki O and March N H 2019 Clifford algebra approach of 3D Ising model *Adv. Appl. Clifford Algebras* **29** 1–28

[27] Bessimou M and Masrour R 2022 Magnetocaloric effect and magnetic properties of $Dy_2CoMnO_6$ : Monte Carlo study *Philos. Mag.* **103** 56–66

[28] El Maazouzi A, Masrour R and Jabar A 2022 Magnetocaloric effects and magnetic properties in A-site cation-ordered chromate LiM(Ga and In) $Cr_4O_8$ spinels *Physica* B **631** 413712

[29] Bessimou M, Masrour R, Jabar A, Kadim G and Hlil E K 2022 Density functional theory and Monte Carlo study of electronic, magnetic and magnetocaloric properties of $Fe_3CoN$ and $FeCo_3N$ antiperovskites *J. Cryst. Growth* **581** 126497

[30] Chen Y H, Tao H S, Yao D X and Liu W M 2012 Kondo Metal and ferrimagnetic insulator on the triangular kagome lattice *Phys. Rev. Lett.* **108** 246402

[31] Wang X J and Jiang W 2022 Static and dynamic magnetic properties in two-dimensional Lieb-like lattice *Chinese J. Phys.* **80** 349–66

[32] Wang C F, Gao W C and Jiang W 2022 Compensation temperature and dynamic magnetic properties in the double-layer structure of graphyne-like *J. Magn. Magn. Mater.* **564** 170122

[33] Shi K L, Quan X W and Jiang W 2023 Study on the magnetic and hysteresis behaviors in a bilayer graphene-like ring with edge decorated *Phys. Scr.* **98** 015822

[34] Jiang Q, Yang N and Wang G C 1995 Scaling and dynamics of low-frequency hysteresis loops in ultrathin Co films on a Cu (001) surface *Phys. Rev.* B **52** 14911

[35] He Y L and Wang G C 1993 Observation of dynamic scaling of magnetic hysteresis in ultrathin ferromagnetic Fe/Au (001) films *Phys. Rev. Lett.* **70** 2336

[36] Acharyya M 2005 Nonequilibrium phase transitions in model ferromagnets: a review *Int. J. Mod. Phys.* C **16** 1631–70

[37] Berger A, Idigoras O and Vavassori P 2013 Transient behavior of the dynamically ordered phase in uniaxial cobalt films *Phys. Rev. Lett.* **111** 190602

[38] Vatansever E and Polat H 2015 Dynamic phase transitions in a ferromagnetic thin film system: A Monte Carlo simulation study *Thin Solid Films* **589** 778–82

[39] Vatansever E 2018 Dynamically order–disorder transition in the kinetic Ising model on a triangular lattice driven by a time dependent magnetic field *Physic* A **511** 232

[40] Ertaš M, Keskin M and Deviren B 2012 Multicritical dynamic phase diagrams and dynamic hysteresis loops in a mixed spin-2 and spin-5/2 Ising ferrimagnetic system with repulsive biquadratic coupling: Glauber dynamic approach *J. Stat. Phys.* **146** 1244–62

[41] Ertaš M, Keskin M and Deviren B 2012 Dynamic magnetic properties in the kinetic mixed spin-2 and spin-5/2 Ising model under a time-dependent magnetic field *Physica* A **391** 1038–47

[42] Ertaš M 2018 Dynamical thermal dependences of the total magnetization and dynamic magnetic hysteresis properties of Ising bilayer system with square lattice *Physica* B **550** 154

[43] Alzate-Cardona J D, Barco-Rios H and Restrepo-Parra E 2018 Dynamic phase transitions in $La_{2/3}Ca_{1/3}MnO_3$ manganites: A Monte Carlo simulation study *Phys. Lett.* A **382** 792–7

[44] Gallardo R A, Idigoras O, Landeros P and Berger A 2012 Analytical derivation of critical exponents of the dynamic phase transition in the mean-field approximation *Phys. Rev.* E **86** 051101

[45] Vatansever Z D 2022 Dynamic phase transitions on the kagome Ising ferromagnet *Phys. Rev.* E **106** 054143

[46] Metropolis N, Rosenbluth A W, Rosenbluth M N, Teller A H and Teller E 1953 Equation of state calculations by fast computing machines *J. Phys. Chem.* **21** 1087–92